Article in Press

Acute deformation characteristics of standard and flexible lithium-ion battery electrodes

Sam Riley, Antonis Vamvakeros, Gustavo Quino, John Morley, Mengzheng Ouyang, Andrew Shevchuk, Kehan Huang, Pierre-Olivier Autran, Stefan Michalik, Genoveva Burca, Billy Wu, Nigel Brandon & Chandramohan George

We are providing an unedited version of this manuscript to give early access to its findings. Before final publication, the manuscript will undergo further editing. Please note there may be errors present which affect the content, and all legal disclaimers apply.

If this paper is publishing under a Transparent Peer Review model then Peer Review reports will publish with the final article.

Acute Deformation Characteristics of Standard and Flexible Lithium-Ion Battery Electrodes

Sam Riley[1], Antonis Vamvakeros[1,2], Gustavo Quino[3], John Morley[4], Mengzheng Ouyang[4], Andrew Shevchuk[5], Kehan Huang[6], Pierre-Olivier Autran[7], Stefan Michalik[8], Genoveva Burca[8,9,10], Billy Wu[1], Nigel Brandon[4], and Chandramohan George[1*]

[1]Dyson School of Design Engineering, Imperial College London, London, SW7 2AZ UK
[2] Finden Ltd, The Oxford Science Park, Magdalen Centre, Robert Robinson Avenue, Oxford OX4 4GA UK
[3]Department of Aeronautics, Imperial College London, London, SW7 2AZ UK
[4]Department of Earth Science and Engineering, Imperial College London, London SW7 2AZ, United Kingdom
[5]Department of Medicine, Imperial College London, London, W12 0NN, UK
[6]Department of Materials, Imperial College London, London, SW7 2AZ UK
[7] ESRF - The European Synchrotron, CS40220, F-38043 Grenoble Cedex 9
[8] Diamond Light Source Ltd, Harwell Science and Innovation Campus, Didcot, Oxfordshire OX11 0DE, UK
[9] Rutherford Appleton Laboratory, ISIS Pulsed Neutron and Muon Source, Harwell Campus, Didcot OX11 0QX, UK
[10] Faculty of Science and Engineering, The University of Manchester, Oxford Road, Manchester M13 9PL, UK

Corresponding Author Email: chandramohan.george@imperial.ac.uk

KEYWORDS: Free standing electrodes, flexibility, synchrotron XRD, Synchrotron nano-CT, folding, electrochemical analysis.

Abstract: Understanding the strain tolerance of both standard and mechanically flexible battery electrodes is prerequisite for optimizing performance, safety, and longevity, particularly in heavy-duty applications, flexible electronics and wearables. Achieving this requires a deeper understanding of how mechanical strain drives electrode degradation. In this work, we directly compare the strain response of electrospun (flexible) and slurry-cast (conventional) electrodes. To simulate acute mechanical stress, electrodes underwent a controlled 180° folding, pressing, and unfolding protocol designed to induce measurable damage, we then employed a combination of characterization techniques, including synchrotron X-ray nano-computed tomography, X-ray diffraction mapping, electrochemical analysis, and in situ Tensiometer-scanning electron microscopy to assess both structural and electrochemical degradation modes and provide a standardised upper-bound for strain induced damage. Our results reveal that electrospun electrodes exhibit significantly greater resilience to deformation, attributed to their freestanding architecture and fibrous morphology.

These findings underscore the importance of characterizing deformation mechanisms to guide the design of high-performance batteries.

INTRODUCTION

As the use of standard lithium-ion (Li-ion) batteries continues to rise, coupled with the emerging application of mechanically flexible batteries in consumer electronics and wearables, understanding the impact of mechanical strain on battery electrodes has become increasingly crucial to ensuring safety, performance and longevity. Flexible batteries [1-4] are vital for enabling wearable electronics and health monitoring devices, catering for a broad range of novel applications powered by batteries. These prospective applications offer valuable benchmarks for electrochemical performance and mechanical deformation of flexible or mechanically durable battery electrodes, enabling electromechanical performance criteria to be established. However, despite nearly two decades of research into flexible batteries, the field has seen only limited success. A significant trade-off between mechanical flexibility and electrochemical performance persists[5], which has hampered the widespread adoption and commercial viability of flexible batteries [6]. Most conventional Li-ion battery electrodes are fabricated using slurry casting, where a slurry comprising electrode active materials, conductive carbon additives, and polymer binders is coated onto metal foil current collectors [7]. These electrodes are inherently prone to deformation, especially when wound into a "jelly roll" configuration for cylindrical cells, with a core diameter of approximately 2 mm [8]. This winding process introduces compressive and tensile stresses that can lead to irreversible changes in both electrochemical and mechanical properties, a phenomenon known as electromechanical damage [9-12]. During winding, the electrode experiences the highest stress concentrations at the center of the jelly roll, where maximum strain occurs at the smallest bending radii. This localised strain maxima results in an increased probability of defect formation at the center of the jellyroll during winding, manifesting as stress concentration sites during cycling-induced volumetric fluctuations, reducing the mechanical failure threshold. In addition, for example silicon[13] is a promising anode material due to its high capacity, but its significant cycling-induced expansion presents challenges to the development of strain-tolerant electrodes that are vital for high-performance batteries. As such, the interplay of mechanical stress and electrochemical performance in slurry cast electrodes requires greater investigation to engineer next-generation cylindrical cells.

For flexible batteries, the electromechanical stability of electrodes is crucial to achieving dynamic stability, meaning that electrochemical performance remains unaffected by mechanical strain. Traditional slurry-cast electrodes fail to withstand repeated bending, as the metallic foil current

collectors are prone to fatigue fractures and delamination from the current collector [14]. To address these challenges, a variety of flexible electrode designs have been explored, such as nano-structured carbon additives [15-17], the use of conductive polymer binder-rich electrodes [18] and carbon paper [19], as well as the use of lithography [20] for catalyst patterns for growing carbon nanotube scaffolds, nano papers [21], biomimetics [22], graphite films [23], 3D electrode design [24] and flexible electrolytes [25]. Despite these innovative lab-scale demonstrations, engineering strain-tolerant electrodes that maintain high electrochemical performance remains a formidable challenge. Strain-induced damage manifests in various forms, including capacity degradation, accelerated aging, and compromised safety. A key difficulty in designing strain-tolerant battery electrodes lies in preserving the integrity of conductive networks. Deformation can disrupt both electrical and ionic percolation within the electrode, leading to capacity loss, failure, or safety hazards. To mitigate this, active materials must remain electrically and ionically accessible across the entire volume of the electrode. Insufficient anchoring of active particles may result in their displacement during bending, while overly large particle sizes may break under strain. Electrospun electrodes [26-28] have been identified as one promising solution due to their high aspect ratio and porous structure, both of which contribute to flexibility and mechanical stability [29]. However, their low mass loading of active materials and potential electrolyte decomposition presents challenges for useable capacity and long-term stability.

Unlike cylindrical cells, flexible batteries are typically manufactured in pouch format, where electrodes are laminated and vacuum sealed. Deformation of the pouch cell imposes less stress on the electrodes than ex-situ bending because the encapsulation and additional layers help prevent delamination by acting as a stress buffer. When bending a layered structure, the outer surface undergoes maximum tensile stress, while the inner surface experiences compressive stress. Therefore, the strain experienced by the electrodes depends on their position within the stack and therefore the thickness of the encapsulation can be tailored to situate the electrodes in a mechanically neutral plane to minimise stress [30]. Maximum strain is often defined as $\varepsilon = h/2r$, where h represents the electrode thickness and r is the bending radius [31]. To resist structural damage during deformation, each material within the stack must exhibit adequate strain tolerance in relation to the imposed bending radius. This highlights the need for thorough electromechanical characterization to quantify the performance of flexible electrodes.

Although electrochemical failure mechanisms in conventional Li-ion batteries are well documented, much less is known about mechanical degradation at the electrode level. Most studies on flexible batteries report deformation at the device scale, often overlooking how localized strain and folding initiate damage within individual electrode layers. This gap limits the rational design of strain-tolerant electrodes for both flexible electronics and mechanically stressed conventional cells. To

address this, we prepared four electrode types—pristine slurry-cast (SC), folded slurry cast (SC-F), pristine electrospun (ES), and folded electrospun (ES-F)—and subjected them to an acute folding protocol. This protocol represents an extreme and localized strain case, chosen as a reproducible proxy for severe deformation rather than a direct simulation of practical operating stresses. By establishing an upper bound for electromechanical damage, it enables systematic comparison of electrode failure mechanisms. By combining electrochemical testing with synchrotron X-ray diffraction, nano-computed tomography, and in-situ SEM-tensile analysis, we directly compare the structural and electrochemical responses of these contrasting electrode architectures and identify by which strain-induced mechanism degradation occurs.

RESULTS AND DISCUSSION

Carbonized electrospun electrodes incorporating LFP (lithium iron phosphate, LiFePO₄) particles are presented in Figure 1 and Methods section (Figure 7) for electrode preparation. Despite the inclusion of LFP particles during the electrospinning process, the particles retained their morphology and crystalline phases following carbonization, as confirmed by SEM-EDX and X-ray analyses (Fig. 1a–c). The LFP mass loading in these electrodes can be tuned by adjusting the electrospinning duration and electrospray flow rate. In the current configuration, the electrodes contain approximately 1.8 mg cm⁻² (≈ 83 wt%, when normalized to the whole electrode) LFP, as determined by thermogravimetric analysis (TGA) [32] (see Supplementary Figure 1). For comparison, the slurry-cast electrodes exhibited a mass loading of ≈ 2.2 mg cm⁻² (≈ 31 wt%, when normalized to the whole electrode), which aligns with typical laboratory-scale values, as 2032-type coin cells are commonly tested within the 1–5 mg cm⁻² range. It should be noted that the reported overall mass loadings include the current collector mass in the case of slurry cast electrodes (~6.7 mg), which reduces the apparent active material fraction to 31% of the electrode as a whole. In contrast, the electrospun electrodes do not contain a metallic current collector, allowing a higher proportion of active material but also introducing greater porosity and redundant volume to provide mechanical compliance. The electrospun electrode loading therefore represents a balance between spinnability, active content, and flexibility. Direct comparison between the two architectures should therefore be made on the basis of areal loading and resistance trends rather than gravimetric capacity, since the presence or absence of a current collector inherently alters the denominator in mass-normalised metrics.

Some agglomeration of LFP is visible in the ES sample, due to the electrospraying process (limited particle dispersion). As the electrospraying solution is electrostatically attracted to the collector, the active material can be dispersed unevenly due to variations in electrostatic field strength and solution inhomogeneity, resulting in pseudo-secondary particles of LFP.
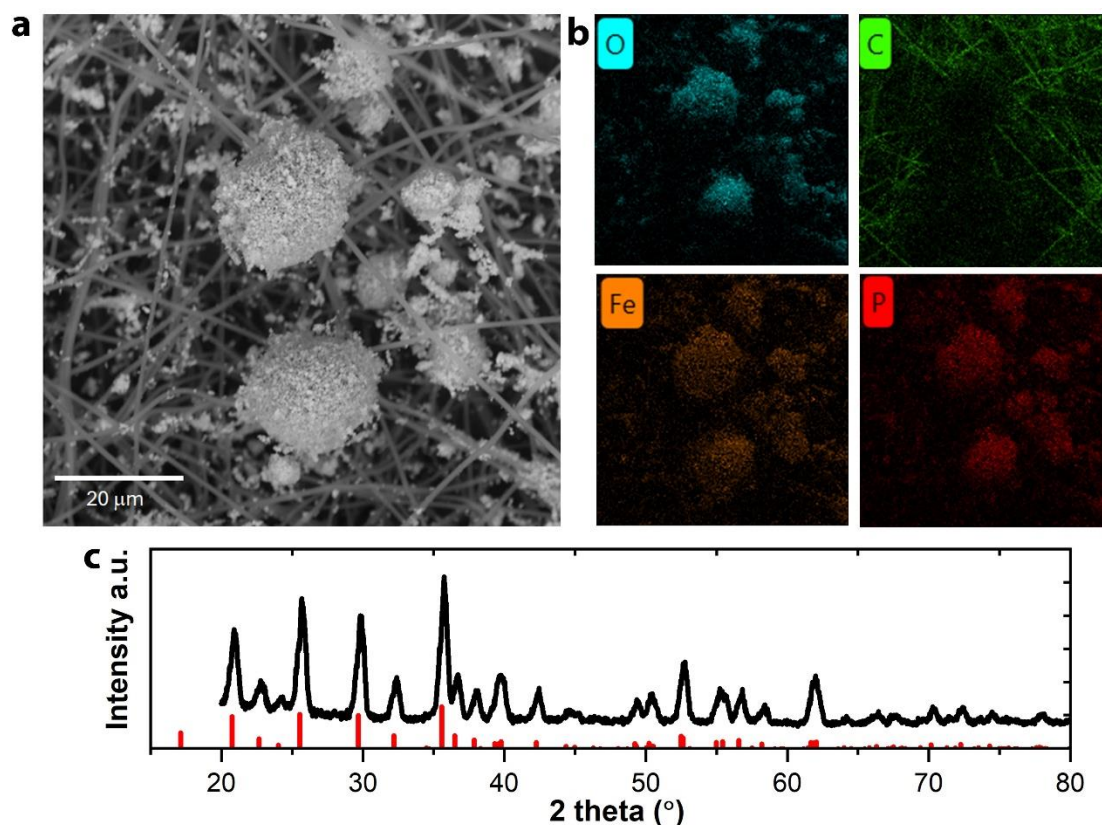
Figure 1. Scanning electron microscopy (SEM), electron dispersive x-ray spectroscopy (EDX) and X-ray diffraction (XRD) analysis of the electrospun cathode. (a) SEM image of the free-standing electrospun and carbonized electrodes containing LFP (ES), showing primary and secondary LFP particles due to agglomeration. (b) EDX mapping of the ES electrode, showing the elemental distribution. (c) XRD pattern of the ES electrode (Cu Kα source), highlighting distinct LFP peaks consistent with the LFP reference standard (REF: 01-081-1173).

Figure 2 shows the electrochemical impedance spectroscopy (EIS) and cyclic voltammetry (CV, scan rate $50\,\mu V\,s^{-1}$) profiles for the slurry-cast (SC; Figure 2a-b) and electrospun (ES; Figure 2c-d) electrodes. The characteristic Fe^{2+}/Fe^{3+} redox peaks of LFP during charge/discharge are evident and align with values reported in the literature [33]. A voltage offset of approximately 0.2V between the anodic (≈ 3.55 V) and cathodic (≈ 3.35 V) peaks is observed for both electrode types, reflecting the intrinsic phase-separating behaviour of LiFePO$_4$. During (de)lithiation, coexistence of LiFePO$_4$ and FePO$_4$ domains leads to transformation at slightly different potentials, producing the characteristic voltage hysteresis [34]. Minor additional peak shifts may arise from differences in carbon content and interfacial reactions with LiFePO$_4$, as uncoated LFP particles exhibit poor intrinsic conductivity and require carbonaceous additives to facilitate charge transfer. Both electrode types demonstrated stable

and reversible cycling. Based on weight calculations, the carbon content was calculated to be approximately 0.27 mg cm⁻² for SC electrodes and ≈ 0.36 mg cm⁻² for ES electrodes based on TGA analysis, the latter being higher due to the presence of a carbon scaffold current collector in place of metallic foil.
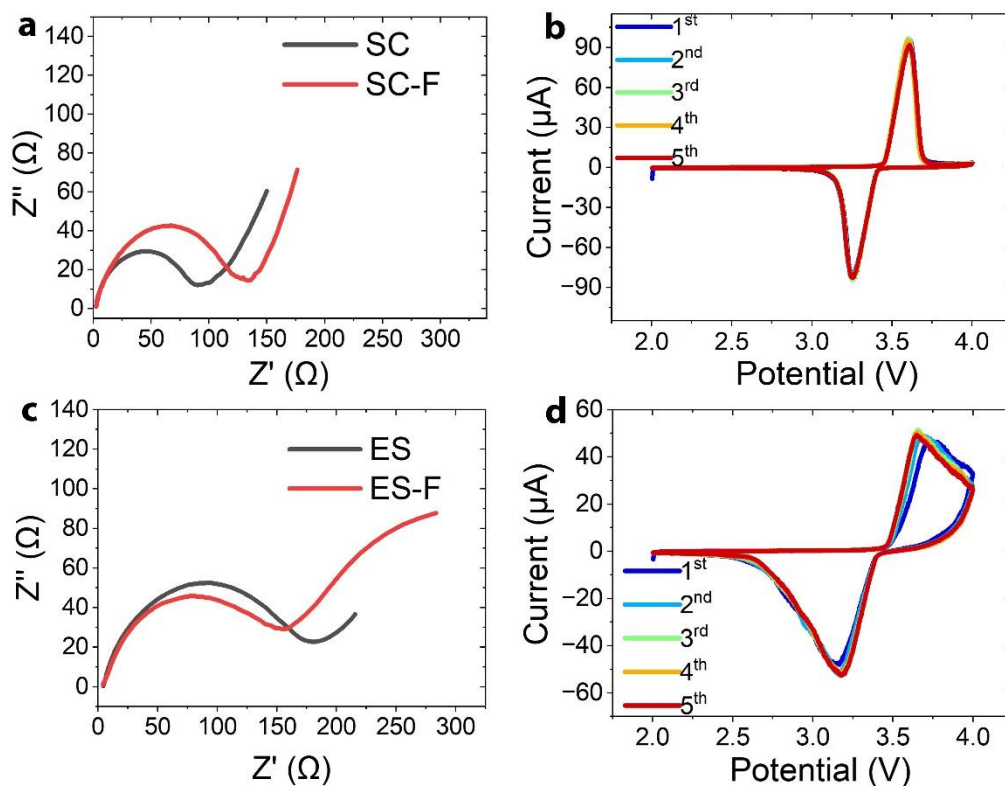

Figure 2. *Electrochemical Characterisation of ES and SC electrodes before and after folding. (a) Electrochemical impedance spectroscopy (EIS) of folded (SC-F) and unfolded (SC) slurry-cast electrodes. (b) Cyclic voltammetry (CV) profile of the SC electrode at a scan rate of 50 μV s⁻¹. (c) EIS of folded (ES-F) and unfolded (ES) electrospun electrodes. (d) CV profile of the ES electrode at a scan rate of 50 μV s⁻¹.*

Figure 2c shows EIS spectra of electrospun electrodes (ES and ES-F), with all measurements conducted in the charged state. Cells were charged at 1C (0.6 mA) to 3.8 V using a constant current–constant voltage (CCCV) protocol (I = 20 μA). Folding and unfolding of the slurry-cast electrodes (SC-F) resulted in a crease visible under SEM, accompanied by ≈ 61% increase in charge transfer resistance (R_{CT}) and ≈ 73% increase to ohmic resistance (R_s) compared to the pristine SC electrode, suggesting microstructural damage induced by a single fold. The EIS spectra were fitted using a modified Randles-de Levie Equivalent Circuit (Supplementary Figure S2). This degradation may stem from various mechanisms, including loss of electronic contact, detachment of active material, layer delamination, and disruption of ionic pathways. In contrast, whilst no creasing was observed in SEM of the electrospun electrodes post-folding; the R_{CT} of ES-

F still increased by ≈ 12.5% and R_s increased by ≈ 7.5% relative to pristine ES, indicating that the strain imposed exceeded the mechanical tolerance of both electrode types. Furthermore, agglomeration of LFP particles in the electrospun electrodes (Figure 1a) reduces the contact area of these pseudo-secondary particles with the conductive fibers, increasing the electron transfer distance to the active material. Notably, electrochemical changes are most severe in the creased region and therefore changes in R_{CT} and R_s are a function of both strain magnitude and the proportion of affected surface area. Optical microscopy (Supplementary Figures 3 and 4) revealed that the deformed region in SC-F is approximately 90 µm wide, corresponding to ≈ 1.35 mm² or ≈ 0.76% of the total electrode area. Whilst this area is relatively small as a percentage of the total area, the electronic pathways and current collector surface are interrupted along the entire length of the electrode, resulting in a reduction of interparticle contact. This is evident by the disproportionate increase in Ohmic and charge transfer resistance resulting from the single fold. Additional effects, such as compression during folding and potential current collector delamination, may also contribute but are not fully discernible via optical imaging.

The relatively modest increase in resistance observed between ES and ES-F electrodes (Figure 2c) may arise from both methodological and structural factors. EIS provides an averaged response across the electrode surface and may not fully capture highly localized disruptions of electronic and ionic pathways within the folded region. Additionally, the electrospraying process can produce inhomogeneous $LiFePO_4$ distributions, including agglomerates, which may reduce sensitivity to localized damage. Another important consideration is the difference between coin cell and pouch cell formats. In coin cells, electrons are delivered uniformly across the electrode surface via a stainless steel disc, allowing regions on either side of a fold to remain accessible. In pouch cells, current is collected from tab ends, meaning electrons must traverse the folded region itself and localized disruption of conductive pathways would therefore have a much greater impact on electrochemical performance. This distinction suggests that the damage observed here would likely manifest more severely in pouch cells than in the coin-cell geometry used in this study.

Capacity-voltage profiles were not included in this work, as their absolute values are dominated by intrinsic formulation differences (e.g. carbon content, porosity, electrode density) rather than by the folding process itself. For electrospun electrodes, acute gravimetric normalization is further complicated by the electrospraying process, where interactions between charged particles and the electrostatic field can produce slight variations in the active material loading per unit area. Although approximate loading values were obtained by destructive TGA analysis, these are specific to the tested specimen and cannot be directly applied to electrodes assembled for electrochemical measurements. Consequently, calculated capacities would be highly sensitive to small loading uncertainties and risk misrepresenting the impact of folding. More critically, capacity after a single acute fold does not provide mechanistic insight into the structural

degradation, as capacity fade may evolve cumulatively and non-linearly (e.g. linear, logarithmic or exponential) under repeated strain. Since the aim of this study was to isolate electrode-level damage mechanisms, we therefore prioritised impedance spectroscopy and structural characterisation, which directly reveal strain-induced failure pathways.

Figure 3a-b shows scanning electron microscopy (SEM) images of the folded slurry-cast (SC-F) and electrospun (ES-F) electrodes, respectively, with the folded region highlighted by a red rectangle. In SC-F (Figure 3a), pronounced mechanical deformation is evident within the creased area, even after a single bending cycle. This is to be expected, as according to $\varepsilon = \frac{h}{2r}$ and approximating r $\approx$ 45µm, the aluminium would be subjected to $\approx$ 16-17% strain, far exceeding the elastic limit of 1.27% [35] and therefore resulting in plastic deformation of the current collector.

In addition, the Al current collector (15 µm thickness) would be subject to cyclic metal fatigue after numerous bending cycles, preventing conventional current collectors in highly flexible batteries. In contrast, the ES-F electrode (Figure 3b) shows no visible damage or cracking. Figure 3c shows a normalized scale factor map of Al for the SC-F electrode, illustrating a notable reduction in diffraction intensity within the folded region, indicative of structural disruption. Figure 3d shows a normalized area of the Gaussian peak corresponding to carbon species in the ES-F electrode, showing no significant variation, suggesting structural preservation post-folding.
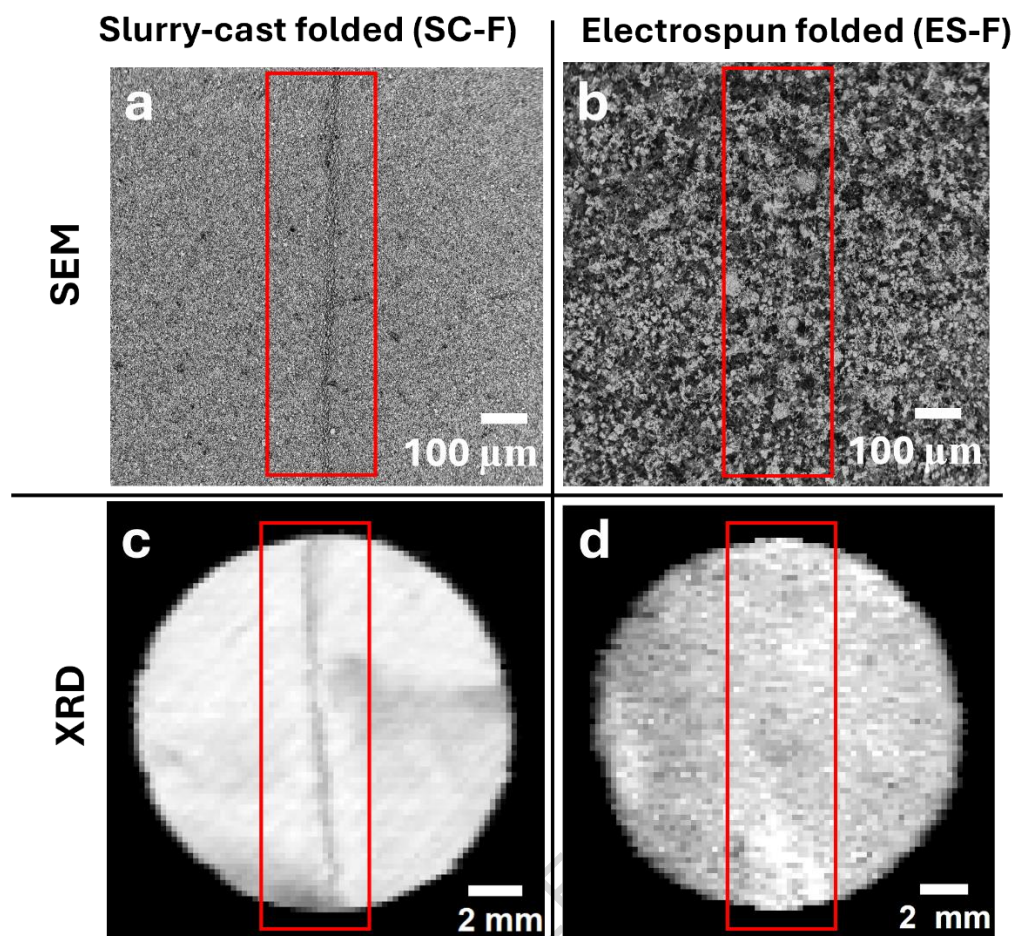
Figure 3. Scanning electron microscopy (SEM) and synchrotron X-ray analysis of deformed electrodes. (a) SEM image of a folded slurry-cast (SC-F) electrode containing lithium iron phosphate (LFP); the red marking highlights the folded region, where visible microstructural damage is observed. (b) SEM image of a folded electrospun (ES-F) electrode, with the red marking indicating the folded area; no visible damage is apparent. (c) Synchrotron 2D X-ray diffraction (XRD) area scan of the SC-F electrode (1.53 cm² region), showing the aluminum (Al) scale factor map; a distinct reduction in Al diffraction intensity is evident in the folded region (red marking), indicating structural disruption. (d) Synchrotron 2D XRD area scan of the ES-F electrode (1.53 cm² region), showing the carbon map; no significant change is observed in the folded area. Full XRD patterns are provided in the Supporting Information (Supplementary Figures 7-11).

X-ray nano-computed tomography (nano-CT) analysis of slurry-cast electrodes before (SC) (Figure 4 a-c) and after folding (SC-F) are presented in Figure 4d-f. Deformation due to folding may

exacerbate current collector delamination, particularly in the absence of encapsulation, which facilitates separation of the electrode layer from the current collector as the electrode is not tightly bound in a vacuum sealed pouch. Post-folding, the SC-F electrode exhibits significant delamination and breakage of the electrode layer, along with distortion of the aluminum current collector (Figure 4d). After isolating the layers, the current collector (Figure 4e) displays a prominent crease along the folded axis, marked by a green rectangle. The corresponding isolated electrode layer (Figure 4f) reveals extensive cracking and breakage along the same axis, also highlighted in green.
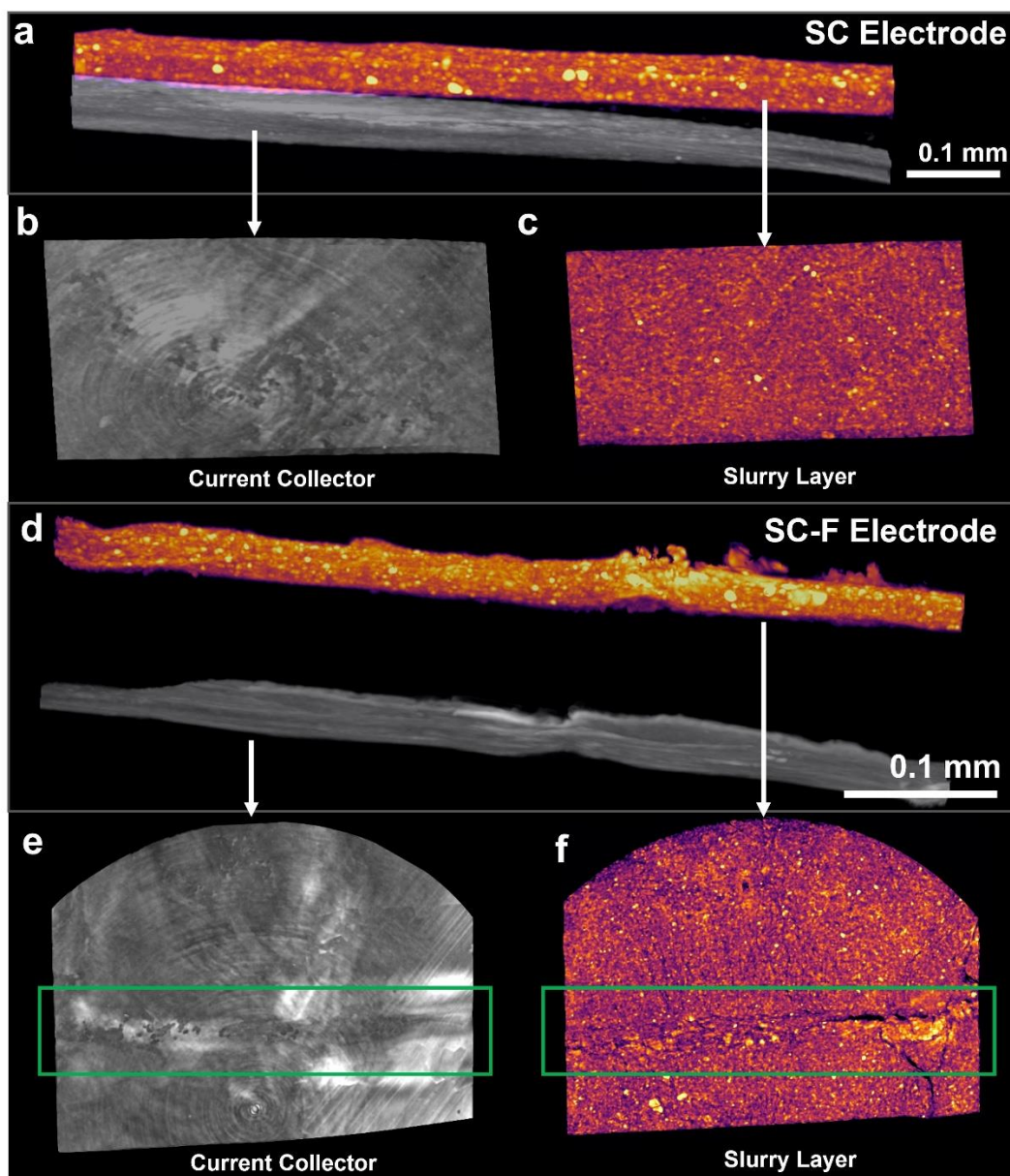
Figure 4. X-ray nano-computed tomography (nano-CT) images of unfolded (SC) and folded (SC-F) slurry-cast electrodes, where brightness intensity corresponds to material density. A red overlay has been applied to the slurry cast layer to distinguish between the grey current collector. Experimental parameters are provided in the Supporting Information (Supplementary Methods 14). (a) Side-view nano-CT image of the unfolded SC electrode, showing the intact slurry layer and current collector. (b) Top-down nano-CT image of the isolated current collector from the SC electrode. (c) Top-down nano-CT image of the isolated slurry layer from the SC electrode. (d) Side-view nano-CT image of the folded SC-F electrode, showing visible deformation. (e) Top-down nano-CT image of the isolated current collector from the SC-F electrode, displaying a distinct crease. (f) Top-down nano-CT image of the isolated SC-F slurry layer, revealing significant cracking and breakage along the folded region.

Figure 5 presents X-ray nano-computed tomography (nano-CT) images of the electrospun electrodes before (ES) and after folding (ES-F). In both Figure 5a and 5b, the upper and lower layers visible in the images correspond to Kapton tape and its adhesive, which were used to sandwich the electrodes during imaging. For clarity, the electrode regions have been outlined with a dashed green rectangle. A comparison between the ES and ES-F samples reveals no visible structural changes following folding, highlighting the mechanical flexibility of electrospun fibers and the advantages of freestanding electrode architectures. This observation is further supported by the top-down nano-CT views of the isolated electrodes (Figure 5c and 5d), which show no evidence of creasing or layer breakage after deformation. These results underscore the importance of current collector selection in the design of flexible batteries, as the use of freestanding electrodes eliminates the risk of current collector delamination. Additionally, numerous pores are visible within the electrospun electrodes. While this porosity facilitates effective electrolyte wetting, it also introduces excess void volume that may reduce the overall energy density compared to more densified electrode structures.
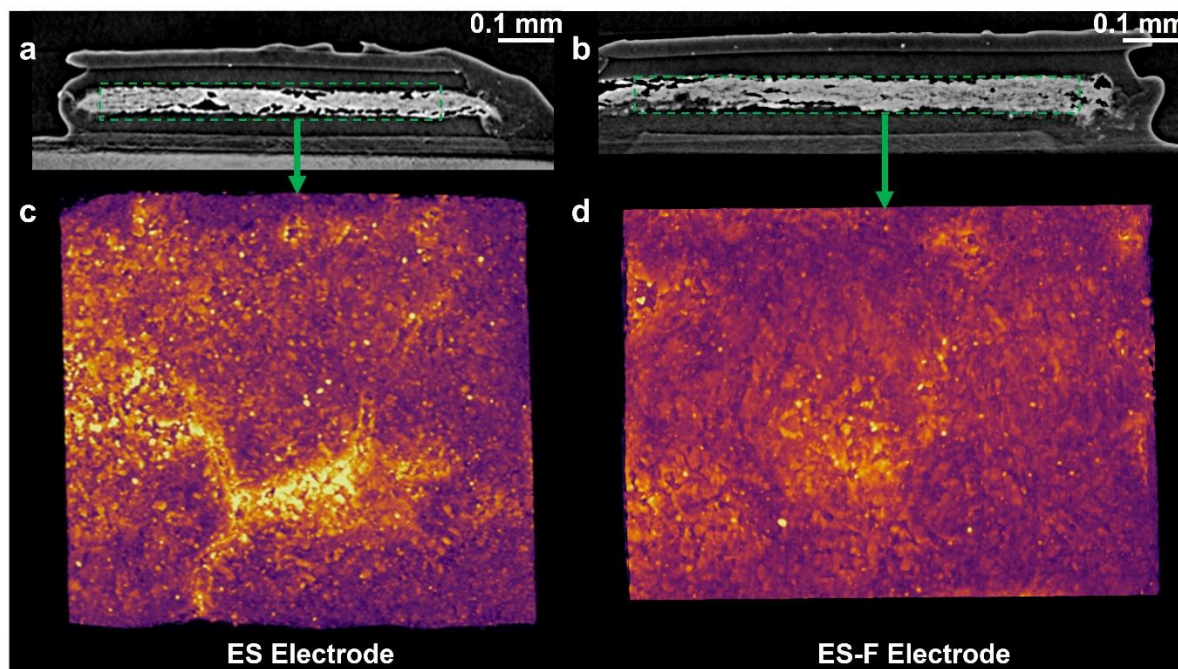
Figure 5. X-ray nano-computed tomography (nano-CT) images of electrospun electrodes before (ES) and after folding (ES-F), where brightness intensity corresponds to material density. Experimental parameters are provided in the Supporting Information (Supplementary Methods 14). (a) Side-view nano-CT image of the unfolded ES electrode. (b) Side-view nano-CT image of the folded ES-F electrode. (c) Top-down nano-CT image of the isolated ES electrode. (d) Top-down nano-CT image of the isolated ES-F electrode.

It should be noted that the folding protocol employed here represents a single, highly localized crease geometry. While this provides a reproducible method for inducing well-defined damage, in practical systems strain may arise from a broader range of deformation modes including multiple crease locations and varying radii of curvature. The crease studied in this work can therefore be regarded as an extreme case of localized strain concentration, analogous to the sharpest bending stresses encountered during electrode winding in cylindrical cells or in sharply folded flexible devices. By deliberately examining the most extreme scenario, we establish an upper bound for electromechanical damage, whilst recognizing that more distributed or less severe strains may yield different degradation pathways.

To investigate the failure mechanisms of the electrodes under mechanical stress, in situ scanning electron microscopy (SEM) was performed during tensile testing using a microtensile rig (Figure 6). Samples of both the slurry-cast (SC) and electrospun (ES) cathodes were prepared in a dogbone

geometry and pre-folded at the center to introduce a crease perpendicular to the main loading axis, following the procedure outlined in Methods Section (Figure 8a, steps 1–4). The samples were subjected to uniaxial tension under displacement control. SEM imaging was conducted at selected displacement intervals to capture the progressive deformation and failure behaviour of the electrodes. The resulting micrographs of the folded SC-F and ES-F electrodes under load are presented in Figure 6a-k.
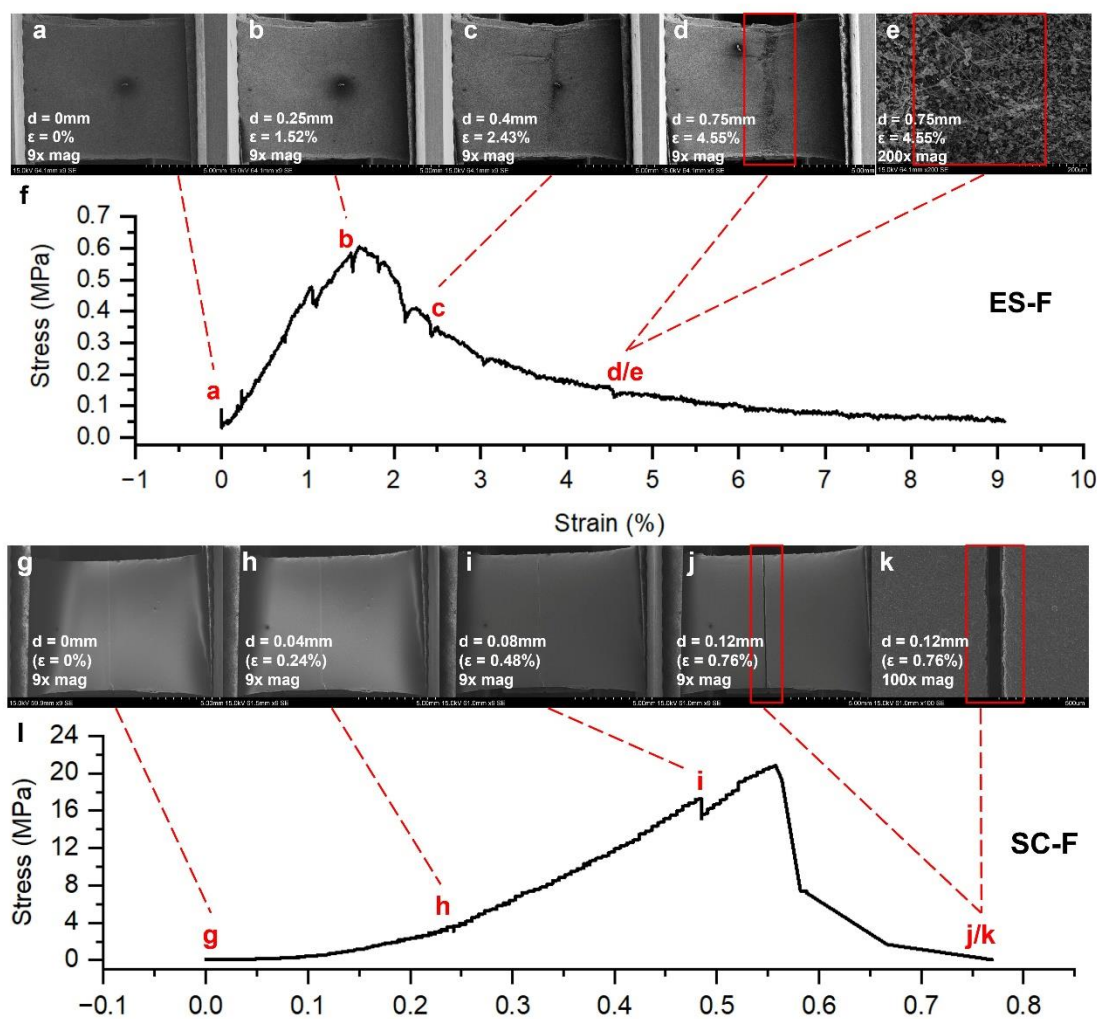

Figure 6. In situ SEM images and corresponding nominal stress–strain curves for electrospun (ES-F) and slurry-cast (SC-F) electrodes under tensile loading, where d = displacement and ε = strain. Motor speed during testing was 0.05mm s⁻¹ for all samples. (a–e) SEM images of the ES-F electrode at increasing displacements and varying magnifications, showing progressive breakage along the folded axis. (f) Stress–strain curve for the ES-F electrode, with a peak stress occurring at approximately

0.35 mm extension, correlating with visible fracture observed in the SEM images. (g–k) SEM images of the SC-F electrode under similar conditions, revealing gradual structural failure along the folded axis. (l) Stress–strain curve for the SC-F electrode, indicating peak stress at approximately 0.9 mm extension, coinciding with the onset of fracture in the SEM images. For comparison, a tensile test was also performed on an unfolded aluminum sample of identical geometry to evaluate the impact of folding on tensile strength (see Supplementary Figure 16). The dog-bone geometry is also shown in Supporting Information (Supplementary Figure 17) .

Figure 6a–f illustrates that, although the electrospun (ES-F) sample fails along the folded axis due to strain induced by folding, electrical connectivity is preserved. SEM images at high displacement (Figures 6d–e) reveal the presence of carbon fiber bridging across the fracture zone, which supports continued electrical conduction despite mechanical failure. This observation is corroborated by the necking behavior observed in the corresponding stress–strain curve (Figure 6f), indicating sustained load-bearing capacity and electrical continuity beyond the onset of structural failure. This bridging effect helps prevent electrical isolation of the active material in the fractured region, enabling the electrode to maintain functionality even after substantial mechanical deformation. In contrast, Figure 6g-k shows the in-situ SEM tensile test results for the slurry-cast electrode (SC-F). Similar to ES-F, SC-F fails along the folded axis, where mechanical damage from folding is localized. However, the failure in SC-F is more brittle in nature, with fracture occurring abruptly at a much lower strain (≈ 0.55%). No fiber bridging is observed, and SEM imaging (Figure 6k) confirms that the electrode separates completely into two electrically isolated segments upon failure. This difference is attributed to the lower ductility of the aluminum current collector compared to the electrospun carbon fibers, as well as microstructural degradation from folding, such as grain boundary migration and grain refinement, further contributing to embrittlement.

The marked difference in peak stress between SC-F and ES-F electrodes can be attributed to their fundamentally different architectures. The SC electrodes consist of a dense slurry coating supported on an Al foil current collector, which dominates the tensile response and results in high apparent stress values. In contrast, the ES electrodes are freestanding fibrous mats with lower density, leading to lower peak stresses but much greater compliance and strain tolerance. This comparison is therefore not intended as a direct equivalence of absolute mechanical performance, but rather to illustrate how distinct electrode architectures respond differently when subjected to identical folding conditions. This interpretation is further supported by the synchrotron x-ray analysis, which confirms architectural differences in load distribution, and by the tensile SEM observations, where the mode of necking reinforces the conclusion that the two electrodes fail via distinct mechanisms.

Additionally, it is important to note that cold rolling of aluminum and copper foils produces anisotropic mechanical properties, which poses challenges for flexible electronics subject to multidirectional strain [36]. Under practical conditions, slurry-cast electrodes are therefore likely to suffer terminal damage even under relatively small strains, resulting in electrical disconnection and device failure. The electrochemical characterisation presented here captures only the immediate effects of acute folding, rather than extended cycling under repeated bending. While this represents a limitation of the current study, the in-situ SEM observations provide mechanistic insight into why the electrospun electrodes maintain function under load. Specifically, the fibrous carbon network forms bridging pathways across fracture sites, preserving electronic connectivity even after severe strain. This structural redundancy explains the modest changes in resistance observed for ES-F electrodes and provides a rational basis for their load bearing capacity. In addition, this study highlights some key characterisation techniques which can be employed to understand the failure mechanisms of flexible electrodes at varying length scales, instead of assessing electrochemical performance as a whole after deformation of the flexible cell. Future studies investigating long-term cycling under mechanical loading will be valuable to confirm the durability of this behavior.

CONCLUSIONS

We have provided a comparative analysis of the mechanical and electrochemical behavior of slurry-cast and electrospun (freestanding) battery electrodes under mechanical deformation. Using a combination of SEM, in situ SEM-tensile testing, electrochemical impedance spectroscopy, synchrotron X-ray diffraction, and X-ray nano-computed tomography, we have elucidated the failure mechanisms and strain responses of these electrodes subject to folding-induced deformation. Our work focused exclusively on the effect of a single acute fold as a proxy for severe electromechanical strain, with the aim of establishing a methodological framework for interrogating electrode-level degradation under mechanical strain. This reveals early degradation pathways that are otherwise hidden in conventional cycling data and provides a blueprint for how future electrode designs, whether for conventional or mechanically flexible batteries, can be systematically evaluated and engineered for mechanical robustness. This includes, in practical manufacturing scenarios such as when cylindrical cell assembly, electrode rolls are inadvertently folded, how such accidental damage can manifest and compromise electrode performance. While repeated folding and cyclic loading would provide further insights into long term durability, in such studies the extent of structural damage rendering electrodes unsuitable for making reliable measurements may be a limitation but represents an important direction for future work. Our findings highlight that the strain tolerance of electrodes is strongly influenced by their microstructural architecture and the directionality of the

applied deformation. Electrospun electrodes, with their inherently anisotropic and fibrous morphology, exhibit superior mechanical resilience and maintain electrical connectivity even after significant strain. In contrast, slurry-cast electrodes experience localized damage and irreversible delamination, particularly at the current collector interface, leading to mechanical failure and electrical isolation. These results underscore the importance of accounting for structural anisotropy and bend axis orientation when designing electrodes for flexible and dynamically deformed battery systems. Moreover, we demonstrate that evaluating mechanical performance at the electrode level prior to full device assembly can offer valuable insights into failure modes and help guide the development of durable, high-performance flexible batteries capable of withstanding complex and repetitive deformation conditions.

METHODS

Two types of cathodes were investigated in this study: slurry-cast (SC) and electrospun (ES) electrodes. The SC electrodes were fabricated using commercially available uncoated lithium iron phosphate, $LiFePO_4$ (LFP, Ossila; particle size ≈ 1.5 µm, D50; nominal specific capacity: 155 mAh g^{-1}). LFP was combined with Super P carbon and polyvinylidene fluoride (PVDF) in a mass ratio of 8:1:1, followed by the addition of N-methyl-2-pyrrolidone (NMP) to form a uniform slurry. This slurry was cast onto 15 µm thick aluminium foil using a doctor blade and left to dry in a fume hood. The dried electrode sheets were then further dried in an oven at 70 °C for 24 hours and subsequently punched into 14 mm diameter discs. For the ES electrodes, a combined electrospinning and electrospraying approach was employed to maximise the active material mass loading. This hybrid method was chosen to overcome the inherent limit on the concentration of non-polymeric particles in spinning solutions, which is governed by particle size, shape, agglomeration tendencies, and the particle-to-fibre diameter ratio [37]. Additionally, electrospraying promotes the anchoring of active particles onto fibre surfaces, enhancing their electrochemical accessibility compared to encapsulation within fibres.

The ES electrodes were fabricated in-house following the process illustrated in Figure 7. The electrospinning solution was prepared by ultrasonically dispersing multi-walled carbon nanotubes (MWCNTs, Sigma; 15 nm diameter, 0.5–10 µm length) in dimethylformamide (DMF, Sigma) for 25 minutes, after which polyacrylonitrile (PAN, Goodfellow; 230 kDa MW) was added and magnetically stirred at 500 rpm and 50 °C for 8 hours, followed by bath sonication to eliminate trapped air and enhance uniformity, then continued stirring for an additional 16 hours (final composition: 0.1 wt% MWCNTs, 10.4 wt% PAN, 89.5 wt% DMF). Separately, the electrospraying solution was prepared

by dispersing LFP powder in DMF via magnetic stirring for 8 hours, followed by the addition of PAN and a further 16 hours of stirring at 50 °C (final composition: 46.5 wt% LFP, 51.8 wt% DMF, 1.6 wt% PAN). The electrospinning process was carried out with a 1 mm spinneret at a flow rate of 1.8 mL h⁻¹, an applied voltage of 19 kV, a spinneret-to-collector distance of 18 cm, and a lateral spinneret translation speed of 18 mm s⁻¹. Electrospraying was performed in tandem under the following conditions: 28 kV, 6 cm collector distance, 1.8 mL h⁻¹ flow rate, and the same lateral movement rate. The solution was deposited onto an aluminium foil substrate mounted on a rotating drum collector (5 cm diameter, 50 rpm). The combined electrospinning/electrospraying process was performed for 60 minutes (30 minutes electrospinning, then introduce co-electrospraying for a further 30 minutes). The resulting fibrous mat was then subjected to thermal treatment, beginning with pre-oxidation at 280 °C in air for 1 hour, followed by carbonisation at 550 °C in a nitrogen atmosphere for 5 hours.

Figure 7. Schematic of the electrode fabrication process with corresponding images of the electrospun mat at each stage. Step 1: Co-electrospinning and electrospraying of PAN/DMF/MWCNT and LFP/DMF/PAN solutions. Step 2: Pre-oxidation at 280 °C for 1 hour (1 °C/min ramp-up, 5 °C/min ramp-down). Step 3: Carbonization at 550 °C for 5 hours (1 °C/min ramp-up, 5 °C/min ramp-down)

Electrospun fibers were carbonized at a relatively low temperature (550 °C) to balance mechanical flexibility and electrical conductivity in the resulting freestanding electrodes [38]. Higher carbonization temperatures promote increased graphitization—reflected by a lower D/G ratio—thereby enhancing electrical conductivity [39]. However, this improvement is offset by increased brittleness arising from mass loss during carbonisation [40]. For the active material, uncoated LiFePO₄ remains structurally stable up to ≈ 900°C, beyond which degradation of the olivine framework occurs [41,42]. The chosen

temperature therefore represents a compromise that avoids LFP degradation whilst minimising brittleness and maximising conductivity in the electrospun cathodes.

To mitigate the reduced conductivity associated with low-temperature carbonization, multi-walled carbon nanotubes (MWCNTs) were incorporated into the electrospinning solution. In contrast to conventional slurry-cast (SC) electrodes, the electrospun (ES) electrodes were expected to retain their conductive pathways under mechanical deformation. This advantage arises from the formation of continuous carbon fiber networks that effectively connect active material particles, coupled with the high porosity of the fibrous mat, which enhances both electrolyte accessibility and mechanical compliance. To introduce a controlled and reproducible fold, a fixed mass was applied across the electrode surface. This approach was chosen to ensure consistency between samples, as manual folding (by hand) would produce variable results. This protocol was not intended to replicate device-level stresses, but to impose a standardised acute deformation that enables comparative analysis of electrode failure mechanisms.

The SC and ES electrodes were manually folded (180°) and pressed under ≈ 1.75 kg (≈ 4.3 kPa) for 10 s to induce a defined crease (bending radius r < 1 mm), then unfolded, yielding SC-F and ES-F samples (Figure 8a). All four electrode types—SC, SC-F, ES, and ES-F—were subsequently assembled into CR2032 half-cells using metallic lithium as the counter/reference electrode for electrochemical testing.

Electrochemical Impedance Spectroscopy (EIS) and Cyclic Voltammetry (CV) were conducted on a PARSTAT MC potentiostat. CV was performed between 2 – 4 V at a scan rate of 50 µV s^{-1}. EIS frequency range was 100 kHz – 0.1 Hz and impedance spectra were fitted using Z-view software with a modified Randles-de Levie equivalent circuit. This comprises solution resistance (R_s), a charge transfer resistance in parallel with a constant-phase element representing the double layer (R_{ct} // CPE_{dl}), and a finite-length transmission line element with short-circuit termination to describe ion transport in porous electrodes. This porous electrode Randles model is widely applied for composite electrodes as it captures both interfacial charge transfer processes and distributed transport effects arising from tortuous porous structures. The same model was used consistently for both slurry-cast and electrospun electrodes to allow direct comparison of their electrochemical response. The equivalent circuit can be found in supporting information (Supplementary Figure 2).

To assess strain-induced changes in electrode structure and current collector integrity, synchrotron-based two-dimensional X-ray diffraction (2D-XRD) was performed on SC-F and ES-F electrodes. Both XRD and X-ray computed tomography (XCT) are established tools for evaluating phase

composition, morphological features, and heterogeneity in battery electrodes, both in situ and ex situ [43,44]. Prior to characterization, cells were discharged at 1C (0.6 mA) to 2 V using a constant current–constant voltage (CCCV) protocol (I = 20 μA), ensuring that the active material was fully lithiated (LiFePO$_4$ phase). The cells were then disassembled in an argon-filled glovebox, and electrodes were sealed in Kapton tape to prevent environmental exposure. The sealed samples were mounted in a custom 3D-printed holder for goniometer analysis (Figure 8a). Details of the XRD acquisition, processing, and analysis procedures are provided in the Supporting Information (Supplementary Methods 5-8). Full-pattern refinement was conducted using TOPAS v7 [45]. For SC-F electrodes, both LiFePO$_4$ and Al phases were modelled, whereas for ES-F electrodes, a Gaussian peak was introduced to capture the broad amorphous carbon background observed at low 2θ values. To visualize nanoscale structural damage caused by mechanical folding, X-ray nano-computed tomography (nano-CT) was performed on all four electrode types. Following 2D-XRD, an approx., 1×1 mm region was excised from each electrode using a sharp scalpel, with folded samples sectioned specifically from the deformed region under a stereomicroscope. The samples were mounted flat on glass substrates and affixed to a goniometer stub for nano-CT analysis (Figure 8b). Detailed acquisition parameters and reconstruction protocols are provided in the Supporting Information (Supplementary Methods 14).
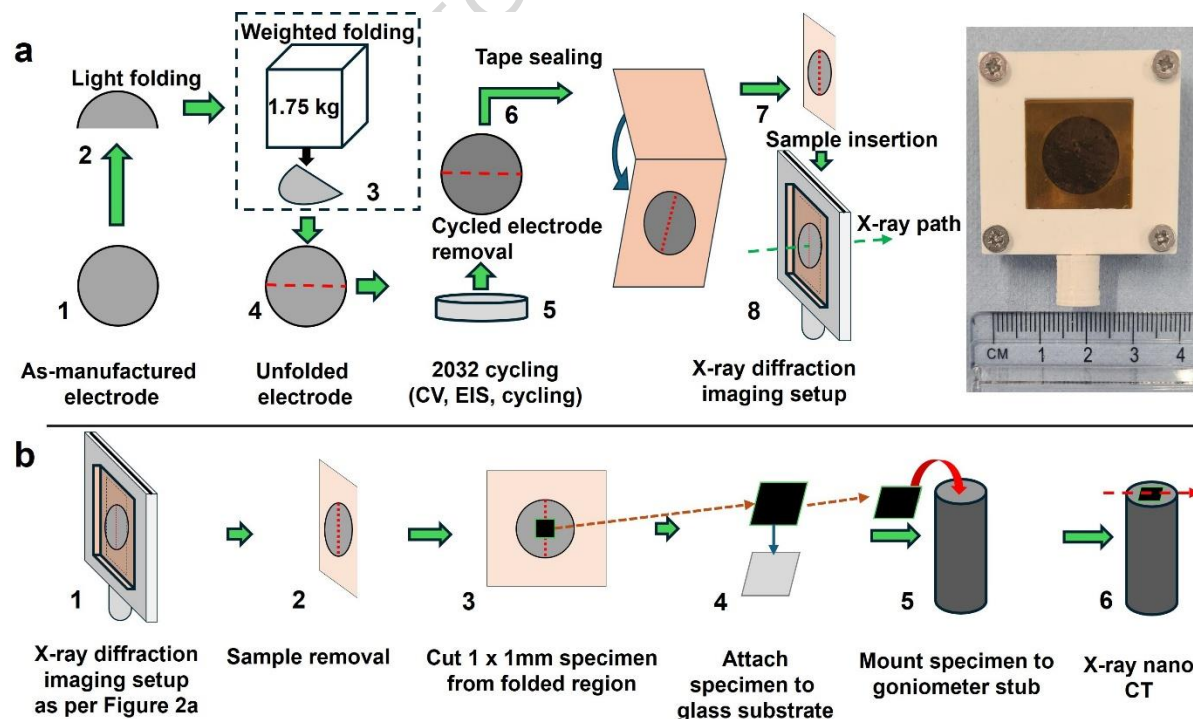
Figure 8. (a) Process diagram illustrating the folding and testing procedures for electrodes prior to assembly into the goniometer mount. (b) Step-by-step workflow for isolating folded specimens from ES, ES-F, SC, and SC-F electrodes.

The thickness of both slurry-cast and electrospun electrodes was approximately 100 μm. According to the relation $\varepsilon = \frac{h}{2r}$[31], a folding scenario with a bending radius of $\approx 45\,\mu m$ would require the electrodes to accommodate a strain of 111% to completely prevent structural damage during deformation.

Corresponding Author

*Chandramohan.george@imperial.ac.uk

Competing interests

The authors declare no competing interest

Author Contributions

S.R and C.G: conceptualization, writing and revision, AV: helped and performed the beamline I12 and ID11 experiments; process of the synchrotron data. G.Q: performed SEM tensiometer testing. J.M.: assisted with synchrotron experiments. M.O: Assistance with electrospinning setup and process. A.S, N.B, B.W: Revision and advice. K.H: Assistance with TGA measurements. P.O.A: assistance with ID11 proposal instrumentation and setup at the ESRF (European Synchrotron Radiation Facility). S.M and G.B.: assistance with I12, proposal, instrumentation and setup at the DLS (Diamond Light Source). All authors: revision.

Data Availability

The data that support the findings of this study are available from the corresponding author upon reasonable request

References

1   https://www.weforum.org/publications/top-10-emerging-technologies-of-2023/.

2   Chang, J., Huang, Q., Gao, Y. & Zheng, Z. Pathways of Developing High-Energy-Density Flexible Lithium Batteries. *Adv. Mater.* **33**, 2004419 (2021). https://doi.org:https://doi.org/10.1002/adma.202004419

3   Wang, S. *et al.* Deformable lithium-ion batteries for wearable and implantable electronics. *Applied Physics Reviews* **9** (2022). https://doi.org:10.1063/5.0117252

4   Zhou, G., Li, F. & Cheng, H.-M. Progress in flexible lithium batteries and future prospects. *Energy & Environmental Science* **7**, 1307-1338 (2014). https://doi.org:10.1039/C3EE43182G

5   Kong, L., Tang, C., Peng, H.-J., Huang, J.-Q. & Zhang, Q. Advanced energy materials for flexible batteries in energy storage: A review. *SmartMat* **1** (2020). https://doi.org:https://doi.org/10.1002/smm2.1007

6   Cha, H., Kim, J., Lee, Y., Cho, J. & Park, M. Issues and Challenges Facing Flexible Lithium-Ion Batteries for Practical Application. *Small* **14**, 1702989 (2018). https://doi.org:https://doi.org/10.1002/smll.201702989

7   Harks, P.-P. R. M. L. *et al.* Immersion precipitation route towards high performance thick and flexible electrodes for Li-ion batteries. *J. Power Sources* **441**, 227200 (2019). https://doi.org:https://doi.org/10.1016/j.jpowsour.2019.227200

8   Waldmann, T., Scurtu, R.-G., Richter, K. & Wohlfahrt-Mehrens, M. 18650 vs. 21700 Li-ion cells – A direct comparison of electrochemical, thermal, and geometrical properties. *Journal of Power Sources* **472**, 228614 (2020). https://doi.org:https://doi.org/10.1016/j.jpowsour.2020.228614

9   Schilling, A., Schmitt, J., Dietrich, F. & Dröder, K. Analyzing Bending Stresses on Lithium-Ion Battery Cathodes induced by the Assembly Process. *Energy Technology* **4**, 1502-1508 (2016). https://doi.org:https://doi.org/10.1002/ente.201600131

10   Kok, M. D. R. *et al.* Virtual unrolling of spirally-wound lithium-ion cells for correlative degradation studies and predictive fault detection. *Sustainable Energy & Fuels* **3**, 2972-2976 (2019). https://doi.org:10.1039/C9SE00500E

11   Pfrang, A. *et al.* Geometrical Inhomogeneities as Cause of Mechanical Failure in Commercial 18650 Lithium Ion Cells. *Journal of The Electrochemical Society* **166**, A3745 (2019). https://doi.org:10.1149/2.0551914jes

12   Gelam, S. D., Maddipatla, S., Chicone, C. & Pecht, M. Core collapse in cylindrical Li-ion batteries. *Journal of Power Sources* **623**, 235471 (2024). https://doi.org:https://doi.org/10.1016/j.jpowsour.2024.235471

13   Cui, Y. Silicon anodes. *Nature Energy* **6**, 995-996 (2021). https://doi.org:10.1038/s41560-021-00918-2

14   Gelb, J., Finegan, D. P., Brett, D. J. L. & Shearing, P. R. Multi-scale 3D investigations of a commercial 18650 Li-ion battery with correlative electron- and X-ray microscopy. *Journal of Power Sources* **357**, 77-86 (2017). https://doi.org:10.1016/j.jpowsour.2017.04.102

15   Gaikwad, A. M. *et al.* A High Areal Capacity Flexible Lithium-Ion Battery with a Strain-Compliant Design. *Advanced Energy Materials* **5**, 1401389 (2015). https://doi.org:https://doi.org/10.1002/aenm.201401389

16   Wei, D. *et al.* Ultra-flexible and foldable gel polymer lithium–ion batteries enabling scalable production. *Materials Today Energy* **23**, 100889 (2022). https://doi.org:https://doi.org/10.1016/j.mtener.2021.100889

17   Hu, L., Wu, H., La Mantia, F., Yang, Y. & Cui, Y. Thin, Flexible Secondary Li-Ion Paper Batteries. *ACS Nano* **4**, 5843-5848 (2010). https://doi.org:10.1021/nn1018158

18   Zhu, T. *et al.* Formation of hierarchically ordered structures in conductive polymers to enhance the performances of lithium-ion batteries. *Nature Energy* **8**, 129-137 (2023). https://doi.org:10.1038/s41560-022-01176-6

19   Zhang, H., Yang, J., Hou, H., Chen, S. & Yao, H. Nitrogen-doped carbon paper with 3D porous structure as a flexible free-standing anode for lithium-ion batteries. *Scientific Reports* **7**, 7769 (2017). https://doi.org:10.1038/s41598-017-07345-y

20   Ahmad, S., Copic, D., George, C. & De Volder, M. Hierarchical Assemblies of Carbon Nanotubes for Ultraflexible Li-Ion Batteries. *Adv. Mater.* **28**, 6705-6710 (2016). https://doi.org:https://doi.org/10.1002/adma.201600914

21   Hu, L. *et al.* Silicon-conductive nanopaper for Li-ion batteries. *Nano Energy* **2**, 138-145 (2013). https://doi.org:https://doi.org/10.1016/j.nanoen.2012.08.008

22   Wang, Y. *et al.* Spider Silk-Inspired Binder Design for Flexible Lithium-Ion Battery with High Durability. *Adv. Mater.* **35**, 2303165 (2023). https://doi.org:https://doi.org/10.1002/adma.202303165

23   Xu, G. *et al.* A High-Energy 5 V-Class Flexible Lithium-Ion Battery Endowed by Laser-Drilled Flexible Integrated Graphite Film. *ACS Applied Materials & Interfaces* **12**, 9468-9477 (2020). https://doi.org:10.1021/acsami.9b22358

24   Han, D.-Y. *et al.* Hierarchical 3D Electrode Design with High Mass Loading Enabling High-Energy-Density Flexible Lithium-Ion Batteries. *Small* **19**, 2305416 (2023). https://doi.org:https://doi.org/10.1002/smll.202305416

25   Kang, S. *et al.* Stretchable Lithium-Ion Battery Based on Re-entrant Micro-honeycomb Electrodes and Cross-Linked Gel Electrolyte. *ACS Nano* **14**, 3660-3668 (2020). https://doi.org:10.1021/acsnano.0c00187

26   Pushparaj, R. I. *et al.* Electrospun Flexible Nanofibres for Batteries: Design and Application. *Electrochemical Energy Reviews* **6** (2023). https://doi.org:10.1007/s41918-022-00148-4

27   Ilango, P. R. *et al.* Electrospun Flexible Nanofibres for Batteries: Design and Application. *Electrochemical Energy Reviews* **6**, 12 (2023). https://doi.org:10.1007/s41918-022-00148-4

28   Yan, Y., Liu, X., Yan, J., Guan, C. & Wang, J. Electrospun Nanofibers for New Generation Flexible Energy Storage. *ENERGY & ENVIRONMENTAL MATERIALS* **4**, 502-521 (2021). https://doi.org:https://doi.org/10.1002/eem2.12146

29   Qian, G. *et al.* Designing Flexible Lithium-Ion Batteries by Structural Engineering. *ACS Energy Letters* **4**, 690-701 (2019). https://doi.org:10.1021/acsenergylett.8b02496

30   Suo, Z., Ma, E. Y., Gleskova, H. & Wagner, S. Mechanics of rollable and foldable film-on-foil electronics. *Applied Physics Letters* **74**, 1177-1179 (1999). https://doi.org:10.1063/1.123478

31   Chang, J., Huang, Q. & Zheng, Z. A Figure of Merit for Flexible Batteries. *Joule* **4**, 1346-1349 (2020). https://doi.org:10.1016/j.joule.2020.05.015

32   Chen, C. *et al.* Microspherical LiFePO3.98F0.02/3DG/C as an advanced cathode material for high-energy lithium-ion battery with a superior rate capability and long-term cyclability. *Ionics* **27**, 1-11 (2021). https://doi.org:10.1007/s11581-020-03796-y

33   <Yu_2007_J._Electrochem._Soc._154_A253.pdf>. https://doi.org:10.1149/1.2434687 ⚹

34   Singh, G. K., Ceder, G. & Bazant, M. Z. Intercalation dynamics in rechargeable battery materials: General theory and phase-transformation waves in LiFePO4. *Electrochimica Acta* **53**, 7599-7613 (2008). https://doi.org:https://doi.org/10.1016/j.electacta.2008.03.083

35   Robinson, W. H. & Truman, S. D. Stress-strain curve for aluminium from a continuous indentation test. *Journal of Materials Science* **12**, 1961-1965 (1977). https://doi.org:10.1007/BF00561967

36   Lee, N. S. *et al.* Anisotropic tensile ductility of cold-rolled and annealed aluminum alloy sheet and the beneficial effect of post-anneal rolling. *Scripta Materialia* **60**, 340-343 (2009). https://doi.org:https://doi.org/10.1016/j.scriptamat.2008.10.036

37   Ewaldz, E., Patel, R., Banerjee, M. & Brettmann, B. K. Material selection in electrospinning microparticles. *Polymer* **153**, 529-537 (2018). https://doi.org:https://doi.org/10.1016/j.polymer.2018.08.015

38   Liu, X. *et al.* In-situ fabrication of carbon-metal fabrics as freestanding electrodes for high-performance flexible energy storage devices. *Energy Storage Materials* **30**, 329-336 (2020). https://doi.org:10.1016/j.ensm.2020.04.001

39   Boll, F. *et al.* Assessing the Effect of Stabilization and Carbonization Temperatures on Electrochemical Performance of Electrospun Carbon Nanofibers from Polyacrylonitrile. *Advanced Energy and Sustainability Research* **4**, 2300121 (2023). https://doi.org:https://doi.org/10.1002/aesr.202300121

40   Yi, S. *et al.* Effects of carbonization temperature on structure and mechanical strength of electrospun carbon nanofibrous mats. *Materials Letters* **273**, 127962 (2020). https://doi.org:https://doi.org/10.1016/j.matlet.2020.127962

41   Ahsan, Z. *et al.* Recent Progress in Capacity Enhancement of LiFePO4 Cathode for Li-Ion Batteries. *Journal of Electrochemical Energy Conversion and Storage* **18** (2020). https://doi.org:10.1115/1.4047222

42   Cai, M. *et al.* Recent advances in synthesis and modification of phosphate-based cathode materials. *Journal of Energy Storage* **95**, 112511 (2024). https://doi.org:https://doi.org/10.1016/j.est.2024.112511

43   Li, W. *et al.* Synchrotron-Based X-ray Absorption Fine Structures, X-ray Diffraction, and X-ray Microscopy Techniques Applied in the Study of Lithium Secondary Batteries. *Small Methods* **2**, 1700341 (2018). https://doi.org:https://doi.org/10.1002/smtd.201700341

44   Deng, Z. *et al.* Recent Progress on Advanced Imaging Techniques for Lithium-Ion Batteries. *Advanced Energy Materials* **11**, 2000806 (2021). https://doi.org:https://doi.org/10.1002/aenm.202000806

45   Coelho, A. TOPAS and TOPAS-Academic: an optimization program integrating computer algebra and crystallographic objects written in C++. *Journal of Applied Crystallography* **51**, 210-218 (2018). https://doi.org:doi:10.1107/S1600576718000183

Editorial summary:

Understanding the strain response of battery electrodes is vital in both standard and flexible devices. Here, the strain response of flexible electrospun, and conventional slurry-cast, electrodes are compared during folding, via x-ray tomography and diffraction, and in-situ microscopy.

Peer review information:

Communications Materials thanks Amit Chanda and the other, anonymous, reviewer(s) for their contribution to the peer review of this work. A peer review file is available.